

# <sup>1</sup> Effects of Electrojet Turblence in simulations of the <sup>2</sup> March 17, 2013 Geomagnetic Storm

M. Wiltberger,<sup>1</sup> V. Merkin,<sup>2</sup> B. Zhang,<sup>1</sup> F. Toffletto,<sup>3</sup> M. Oppenheim,<sup>4</sup> W. Wang,<sup>1</sup> J. G. Lyon,<sup>5</sup> J. Liu,<sup>1</sup> and Y Dimant<sup>4</sup>

---

Corresponding author: M. Wiltberger, National Center for Atmospheric Research, High Altitude Observatory, 3080 Center Green, Boulder, CO 80301 (wiltbemj@ucar.edu)

<sup>1</sup>High Altitude Observatory, National  
Center for Atmospheric Research, Boulder,  
Colorado, USA.

<sup>2</sup>Applied Physics Laboratory, Johns  
Hopkins University, MD, USA.

<sup>3</sup>Department of Physics and Astronomy,  
Rice University, TX, USA.

<sup>4</sup>Center for Space Physics, Boston  
University, Boston, Massachusetts, USA

<sup>5</sup>Department of Physics and Astronomy,  
Dartmouth College, Hanover, NH, USA.

- <sup>3</sup> **Abstract.** Examines the impacts of including Electrojet Turbulence (ET)
- <sup>4</sup> in simulations of to the geomagnetic storm that occurred on 17 March 2013.
- <sup>5</sup> We see many cool things.

## 1. Introduction

6 Initial drafting of this section has been assigned to Meers and Slava.

## 2. Simulation Setup

7 This study focuses on using the geomagnetic storm that occurred on 17 March 2013  
8 as a case study for two new features of the LFM-RCM geospace model. As previously  
9 discussed the LFM-RCM model combines the Lyon-Fedder-Mobarry MHD model of the  
10 magnetosphere with the Rice Convection Model of the inner magnetosphere and the  
11 Mangetosphere-Ionosphere Coupler Solver of ionospheric electrodynamics to provide a  
12 tightly coupled model of the geospace system. *Pembroke et al.* [2012] describes in detail  
13 the basic process of coupling these three models together during idealized solar wind con-  
14 ditions with modest solar wind driving and no dipole tilt. Section 2.1 describes how this  
15 approach has been modified to include realistic solar wind conditions, including nonzero  
16 IMF  $B_Y$ , as well as variations in the Earth's dipole tilt. *Merkin et al.* [2005] implemented  
17 an adjustment to the ionospheric conductances based upon the theoretical analysis of the  
18 Farley-Buneman instability (FBI) conducted by *Dimant and Milikh* [2003]. This capabil-  
19 ity has not been widely used in LFM simulations, but is being made part of the LFM-RCM  
20 geospace model. Section 2.2 discusses how both the Anomalous Electron Heating (AEH)  
21 and Non-Linear Current (NLC) aspects of the Electrojet Turbulence are implemented in  
22 the MIX portion of the LFM-RCM model. Next we present the results of simulations  
23 for a geomagnetic storm that occurred on 17 March 2013. We compare and contrast the  
24 results of LFM-RCM simulations with and without the Electrojet Turbulence including

<sup>25</sup> comparisons with a range of observations. The final section of the paper we discuss our  
<sup>26</sup> results and next steps.

## 2.1. LFM-RCM

<sup>27</sup> *Pembroke et al.* [2012] provides a detailed description of the coupling process between the  
<sup>28</sup> LFM, MIX and RCM models for simulations of geospace. Since that study used idealized  
<sup>29</sup> solar wind conditions with no dipole tilt after reviewing the basics of the LFM-RCM  
<sup>30</sup> coupling this section will address the changes made to coupling infrastructure needed to  
<sup>31</sup> allow model to work for realistic solar wind conditions and dipole tilts.

<sup>32</sup> The fundamental aspect of the model coupling is an exchange of magnetic field and  
<sup>33</sup> plasma information in the inner magnetosphere to RCM from LFM and then an update  
<sup>34</sup> of the plasma information from RCM to the LFM. The MIX model is providing ionospheric  
<sup>35</sup> potential information to both the LFM and RCM models. All of the exchanges use the  
<sup>36</sup> Center for Integrated Space Weather Modeling (CISM) coupling infrastructure and that  
<sup>37</sup> infrastructure is utilized in the update version [*Goodrich et al.*, 2004]. To transfer informa-  
<sup>38</sup> tion from the LFM to the RCM the LFM computes time averages of the pressure, density  
<sup>39</sup> and magnetic field over an exchange interval. The averaged fields are interpolated onto  
<sup>40</sup> an intermediate regular Cartesian grid. This intermediate grid is then used to calculate  
<sup>41</sup> field line-averaged pressure and density for positions in the RCM's ionospheric grid. A key  
<sup>42</sup> innovation of the *Pembroke et al.* [2012] was the implementation of the plasma- $\beta$  method-  
<sup>43</sup> ology for setting the location of the outer boundary of the RCM. This switch, which  
<sup>44</sup> essentially prevented the RCM from computing regions with large flows, remains active  
<sup>45</sup> in the storm simulations we present in this paper. After the RCM computes its plasma  
<sup>46</sup> pressures and densities these values are transferred back to the LFM once again using

47 the intermediate grid. The RCM density model includes a modifications to a fit of static  
48 plasmasphere model of *Gallagher et al.* [2000]. At this time we have not implemented a  
49 dynamic plasmasphere calculation, but that is logical next step for improvement of the  
50 coupled model. Another set of field line traces from the RCM ionospheric grid points are  
51 used to determine the local values on intermediate grid and than those values are inter-  
52 polated to LFM grid points. The mapping back to LFM assumes that the distribution  
53 of plasma density and pressure is constant along field lines. As before the RCM values  
54 do not immediately replace the LFM values, instead they bled into the LFM over the  
55 exchange time interval. It is important to note that the previous work used a 1-minute  
56 exchange interval as a balance between speed and accuracy. For strong solar wind driving  
57 conditions we have found it necessary to reduce the coupling interval to 15-seconds.

58 The first major modification to the previous coupling efforts is in support of including  
59 dipole tilts in the calculation of the coupled model. The LFM-MIX model has long had  
60 support for conducting simulations with realistic dipole tilts. This is done by continuing to  
61 have the dipole axis of the Earth aligned with the Z-axis of the computational model and  
62 inputing the solar wind conditions in SM coordinates. As *Hapgood* [1992] explains the SM  
63 coordinate system has the Z-axis parallel to the north magnetic pole and transformation  
64 between this coordinate system and the more commonly used GSM coordinate system is  
65 simply rotation about the Y-axis by the dipole tilt angle. The cartesian intermediate grid  
66 is setup in SM coordinates for the transfer of data to and from the LFM to RCM the  
67 ionospheric foot points are transformed from geographic coordinates to SM coordinates  
68 using the GEOPACK coordinate transform package. The RCM typically includes the

69 effects of the corotation potential which is not part of stand alone LFM-MIX, but is  
70 enabled when coupled with the RCM.

71 The second key modification of the LFM-RCM coupling is how the asymmetries in the  
72 ionosphere are addressed. In the MIX module the ionospheric potential for the northern  
73 and southern hemispheres are calculated independently. The field-aligned current patterns  
74 taken from the global MHD simulation are shared between the hemispheres, but the  
75 ionospheric conductances can be different. The first major difference comes from the  
76 implementation of a EUV conductance model that calculates the local value of the Hall  
77 and Pedersen conductance based upon the solar zenith angle and the F107 flux value. We  
78 have adapted the approach used by Assimilative Mapping of Ionospheric Electrodynamics  
79 (AMIE) for the MIX module [Richmond, 1992]. The ionospheric conductance model also  
80 includes an empirical model for electron precipitation. As described by Wiltberger *et al.*  
81 [2009] this model includes modifications of the precipitation values based upon the local  
82 EUV conductance values allowing the model to simulate seasonal variations of particle  
83 precipitation and their impacts on geospace system. On the other hand the RCM assumes  
84 that there are no differences between the northern and southern hemispheres.

85 The compromise solution we have adopted for the version of the coupled simulations  
86 present here works as follows. The low latitude boundary of the the ionospheric solu-  
87 tion for electrodynamic solver is extended equatorward from 45° to 60° colatitude. The  
88 45° boundary corresponds to dipole mapping of the 2  $R_E$  inner boundary of the MHD  
89 solution grid within the LFM. The 60° boundary corresponds to the low latitude bound-  
90 ary for the RCM ionospheric calculation. *Frank - Is the previous statement correct?* For  
91 the northern hemisphere the typical low latitude boundary condition of assuming that

92 potential is zero is used. The northern hemispheric values for the potential as well as the  
93 average energy and flux of precipitating electrons are then stored for latter passage to the  
94 RCM for its calculation. The computation of the southern hemisphere potential is done  
95 down  $45^{\circ}$  with the low latitude boundary value being set of the potential obtained from  
96 the northern hemisphere at that location. By setting the southern hemisphere boundary  
97 with the northern hemisphere values we are attempting ensure that closed field lines in  
98 the calculation have the same potential values. *Slava and Frank - Is that the best way to*  
99 *describe the motivation for this coupling approach? Also, should we address why we aren't*  
100 *passing any kind of aggregate flux or conductance information to the RCM calculation.*

101 As a quick side note we take a moment to compare our approach that utilized by  
102 other groups to couple global MHD models with the RCM. The Space Weather Modeling  
103 Framework Tóth *et al.* [2005] to couple the MHD magnetosphere solution to inner mag-  
104 netosphere models. De Zeeuw *et al.* [2004] did the initial work coupling the RCM with  
105 the BATS-R-US magnetosphere solution. Like us they used field line tracing to compute  
106 flux tube quantities for transfer between the two components and also assume the plasma  
107 parameters are constant along field lines. They support exchange intervals between 10  
108 seconds to 10 minutes with the choice of exchange intervals between models being driving  
109 by the strength of convection within the event being simulated. This initial work was  
110 done for simulations with no dipole tilts and uniform ionospheric conductances. Welling  
111 and Ridley [2010] presents validation studies comparing the magnetic field and plasma  
112 parameters for a set of geomagnetic storms. While these results clearly include the effects  
113 of dipole tilts and particle precipitation effects the study does not provide any details on  
114 how these conditions are handled in the coupled model. More recently Glocer *et al.* [2013]

documented the two-way coupling of the Comprehensive Ring Current Model (CRCM) with the BATS-R-US global magnetosphere model, while they presented results for 22 July 2009 geomagnetic storm the paper does not discuss the details of how dipole tilt is addressed. *Frank and Slava - I thought this was a worth while addition here and not in the introduction since it concentrates on coupling details. Am I being to harsh in my language about not discussing how the dipole tilt is addressed? I'm not aware of any OpenGGCM publications with RCM. If I've missed something please let me know.*

## 2.2. Electrojet Turbulence Implementation

*Dimant and Oppenheim [2011]* developed a model of how FBI turbulence modifies E-region conductivities when driven by strong DC electric fields. This turbulence gives rise to both nonlinear currents (NC) and anomalous electron heating (AEH). Both these will increase the conductivities. This model was incorporated into the MIX module as a set of conductance correction factors that depend on the driving electric field.

The model of AEH was developed in *Dimant and Milikh [2003]* assuming a specific FBI turbulence level. This self-consistent approach accounts for the fact that as the FBI turbulence raises the electron temperature  $T_e$ , it increases the instability threshold field,  $E_{\text{Thr}}^{\min}$ , causing the saturated turbulence level to grow with  $E_0$  much more slowly than if  $T_e$  were constant. It also accounted for kinetic modification of the electron distribution function and the corresponding enhanced cooling this causes. The resulting elevated electron temperature  $T_e$  increases the conductivities by reducing in the local plasma recombination rate and therefore increasing the plasma density *Gurevich [1978]; St Maurice [1990]; Dimant and Milikh [2003]; Milikh et al. [2006]*.

<sub>136</sub> The NC model was developed by *Oppenheim* [1996, 1997]. This predicts a strong current  
<sub>137</sub> driven by FB turbulence in the direction of the DC field. The model used in the MIX  
<sub>138</sub> module combines  $E_{\text{Thr}}^{\min}(E)$  with an assumed level of saturated FBI density fluctuations  
<sub>139</sub> as seen in simulations by *Oppenheim and Dimant* [2013]. This modifies the Hall and  
<sub>140</sub> Pedersen conductance, as described in *Dimant and Oppenheim* [2011].

<sub>141</sub> Inside the MIX module we have implemented the following conductance correction terms  
<sub>142</sub> combining the AEH and NC correction factors. In regions where the electric field is greater  
<sub>143</sub> than 35 mV/m we have implemented,

$$\Sigma_P^{ET} = \Sigma_P^O(1 + 0.01(E - 35) + 1.3e10^{-5}(E - 35)^2), \quad (1)$$

<sub>144</sub> as the calculation for the Electojet Turbulence (ET) modified conductance,  $\Sigma_P^{ET}$ . In  
<sub>145</sub> Equation 1  $E$  is the ionospheric electric field in mV/m and  $\Sigma_P^O$  is the Pedersen con-  
<sub>146</sub> ductance obtained from the baseline ionospheric model and includes both the EUV and  
<sub>147</sub> electron precipitation terms. This multiplier includes the effect of the temperature driven  
<sub>148</sub> recombination reduction as well as the that of nonlinear current. The FBI modified Hall  
<sub>149</sub> conductance,  $\Sigma_H^{ET}$ , is simply

$$\Sigma_H^{ET} = \Sigma_H^O(1 + 0.01172(E - 35) - 1.207e10^{-5}(E - 35)^2), \quad (2)$$

<sub>150</sub> where  $\Sigma_H^O$  is the baseline Hall conductance. Figure 1 shows the effects of these multipliers  
<sub>151</sub> over a range electric fields. The Pedersen multiplier (blue curve) is nearly linear over the  
<sub>152</sub> range from 35-200 mV/m reaching a peak value of 3.0 at 200 mV/m. The Hall multiplier  
<sub>153</sub> has a negative coefficient on the squared term and so falls off more dramatically at  
<sub>154</sub> higher values of the electric field. It reaches a value of 2.3 at 200 mV/m. We note that the

<sub>155</sub> Farley-Buneman Instability typically starts developing if the convection field,  $E$ , exceeds  
<sub>156</sub>  $\approx 20$  mV/m. However, the macroscopic effect of E-region turbulence becomes substantial  
<sub>157</sub> only for field when it exceeds  $E > 35$  mV/m, therefore we eliminate the effect below this  
<sub>158</sub> level for computational simplicity.

### 2.3. 17 March 2013 Simulation

<sub>159</sub> On 17 March 2013 an interplanetary coronal mass ejection arrived at the Earth and  
<sub>160</sub> drove a significant geomagnetic storm,  $D_{ST} < -100$ , over the next day. Solar wind con-  
<sub>161</sub> ditions obtained from the OMNI dataset were used to drive the LFM-RCM model and  
<sub>162</sub> those are shown in Figure 2. Prior to the shock preceding the CME the solar wind con-  
<sub>163</sub> ditions are fairly typical, namely density  $\approx 5$  cc, velocity  $\approx 425$  km/s, with interplanetary  
<sub>164</sub> magnetic field (IMF) weak,  $< 5$  nT in magnitude, mainly in the northward direction. At  
<sub>165</sub> 05:55 UT a shock is clearly present in the solar wind with  $V_X$  GSM reaching -650 km/s  
<sub>166</sub> and the density increasing to 10 cc. In the next three hours the IMF is variable, with  
<sub>167</sub> IMF  $B_Z$  mainly southward reaching values of -20 nT, but having significant intervals with  
<sub>168</sub> northward IMF. The Y component of the IMF has similar magnitude in amplitude and  
<sub>169</sub> appears to have a 180 deg phase shift. After approximately 09:00 UT on the 17th the Y  
<sub>170</sub> and Z components become more in phase and slowly reduce in amplitude reaching typical  
<sub>171</sub> values by the end of the day. After about 12:00 UT the solar wind speed slowly begins to  
<sub>172</sub> decrease reaching a value of about 550 km/s by the end of 17 March.

<sub>173</sub> The LFM-RCM simulations for this interval were run using solar wind conditions  
<sub>174</sub> from Figure 2. As previously discussed the LFM uses a non-orthogonal spherical mesh  
<sub>175</sub> for the grid. The simulations conducted here use 106 radial, 96 azimuthal, and 128 polar  
<sub>176</sub> cells. This quad resolution version of the LFM contains twice as many cells as the results

<sup>177</sup> reported by *Pembroke et al.* [2012] initial work with coupling LFM-RCM. The RCM  
<sup>178</sup> simulations where done on a grid with XX and YY points. The intermediate transfer  
<sup>179</sup> grid between LFM-RCM used for the field line tracing had a resolution of ZZ. In the  
<sup>180</sup> MIX ionospheric solution the ionospheric resolution was increased from a 2x2° resolution  
<sup>181</sup> to 1x1°resolution. The full ionospheric conductance model described by *Wiltberger et al.*  
<sup>182</sup> [2009] by was enabled in the MIX calculations. We ran two sets of simulations. The first  
<sup>183</sup> hereafter, baseline, used the standard ionospheric model. The second, hereafter ET, had  
<sup>184</sup> the Electrojet Turbulence implementation discussed in Section 2.2 enabled. The solar  
<sup>185</sup> wind driving, grid resolution, and all other model parameters are not changed between  
<sup>186</sup> these two runs.

### 3. Analysis of results

<sup>187</sup> We now move on to present the results of from the two simulations for the St Patrick's  
<sup>188</sup> Day 2013 storm event. We begin, in Section 3.1, with a broad overview of the results of the  
<sup>189</sup> simulation including comparisons of ionospheric structures and global measures. After this  
<sup>190</sup> overview of the event and simulation results we move onto make comparisons between the  
<sup>191</sup> simulation results and observations. In Section 3.2 we make detailed comparisons between  
<sup>192</sup> the simulation results and Defense Meteorological Satellite Program (DMSP) observations  
<sup>193</sup> during the peak of the storm. These results show ability of the model capture features  
<sup>194</sup> associated with Sub-Auroral Polarization Streams (SAPS). Next, we assess the ability of  
<sup>195</sup> the model to simulate field aligned currents (FACs) by compare the results with patterns  
<sup>196</sup> obtained from the AMPERE mission. Finally, in Section 3.4 we examine the structure  
<sup>197</sup> of the inner magnetospheric pressures associated with the ring current by comparing the  
<sup>198</sup> results with those obtain from the TS07-D empirical magnetic field model.

### 3.1. Baseline versus ET

Figure 3 is frame extracted from the scientific visualization that is included in auxiliary materials that are part of the online version of this article. The top row figure shows the results from the baseline simulation while the bottom row shows the results from ET simulations. Panels a) and d) of Figure 3 provide a comparison between the cross polar cap potential patterns and the structure of the field aligned currents for the northern hemisphere during the course of the magnetic storm. In the snapshot taken at 10:00 UT on March 17th the region-1 and region-2 FAC current structures are clearly apparent. The cross polar cap potential is weaker in the ET run, but the alignment of the pattern in confinement to high-latitudes by the region-2 currents is consistent in both simulation results. The second column, panels b) and e), shows the Pedersen conductance. In both runs the EUV ionization profile is apparent on the dayside along with auroral oval structure driven by the empirical precipitation model. It's also clear at this snapshot that the ET model is having an impact because the Pedersen conductance in the auroral oval is larger in the ET results. The final column of Figure 3, panels c) and f), provides a comparison between the Hall conductances. Just like in Pedersen conductance the EUV profile and auroral oval are apparent. It is important to note that when comparing the conductance plots that color ranges are the same across simulations for each type of conductance, but the Hall conductance upper limit is a factor of two larger than the Pedersen conductance in order to make the differences between the different simulations more apparent.

Before moving on to examine the evolution of the ionospheric parameters in the simulation during the course of the magnetic storm we turn our attention to Figure 4 that shows

221 a comparison of several global diagnostic parameters over the course of the storm. The  
222 top panel, a), shows the time history of the cross polar cap potential obtained by taking  
223 the difference of the max and min of the potential at each dump step. Using a convention  
224 that will be maintained throughout this paper the baseline simulation results are shown  
225 with the green line and the ET simulation results are shown with the purple line. The  
226 second panel, b), of the Figure shows the strength field-aligned current obtained by inte-  
227 grating the positive FAC over the northern hemisphere at each time step. Panel c) at the  
228 bottom of Figure 4 shows a comparison between the simulation results and observations  
229 for the  $D_{ST}$  index. The simulated  $D_{ST}$  index was calculated using Biot-Savart method  
230 that determines the ground magnetic field perturbations driven by the magnetospheric,  
231 field-aligned, and ionospheric currents. Also shown in this panel is observed  $D_{ST}$  index  
232 obtained from CDAweb database. Following the convention for this paper the observed  
233  $D_{ST}$  index is shown with a blue line.

234 The solar wind conditions prior to the 05:50 UT arrival of the shock preceding the  
235 CME are modest with velocity around 420 [km/s], density slight above 3 [cc] and the  
236 IMF mainly northward with a small  $B_Y$  component. The scientific visualization of the  
237 ionospheric parameters begins at 00:00 UT on March 17th and results shown between  
238 then and the arrival of the shock show little difference between the two simulations. For  
239 example at 03:00 UT both simulations show a NBZ current system in the ionosphere  
240 with very weak convection patterns. The main conductance is coming from the EUV  
241 ionization and the maximum conductance values in both simulations are identical. In  
242 looking at the global diagnostic parameters plotted in Figure 4 the lines for the two  
243 simulations are virtually indistinguishable from each other during this interval. This is

<sup>244</sup> inline with our expectations that the ET affects will not be activated during typical solar  
<sup>245</sup> wind conditions.

<sup>246</sup> After the arrival of the shock the velocity exceeds 625 [km/s] with an initial period of  
<sup>247</sup> strongly northward IMF followed by a roughly 40 minute interval of strongly southward  
<sup>248</sup> IMF. Between 6:20 and 7:00 UT the IMF  $B_Z$  component is less than - 10 nT. Combined  
<sup>249</sup> with the high solar speed, this leads to large cross polar cap potentials. The time history  
<sup>250</sup> of CPCP and FAC in Figure 4 show for the first time significant differences in this interval.  
<sup>251</sup> On average the CPCP is 12.7 percent smaller in the ET run than the baseline simulation  
<sup>252</sup> in this interval. This shows that the inclusion of the ET is having the intended effect  
<sup>253</sup> of reducing the CPCP during strong driving conditions. Interestingly, during the same  
<sup>254</sup> interval the FAC is 9.6 percent larger in the ET run than the baseline simulation. This  
<sup>255</sup> shows that there is tight coupling in magnetosphere-ionosphere system and one cannot  
<sup>256</sup> consider the effects of changes in one region in isolation. Looking more closely at the  
<sup>257</sup> scientific visualization at 07:00 UT one sees that the most significant differences between  
<sup>258</sup> the simulated conductances are occurring for the Hall conductance with maximum value  
<sup>259</sup> 20 percent higher in the ET run. This enhanced conductance occurs over the most of the  
<sup>260</sup> auroral oval being most pronounced in the regions near midnight. It's worth pointing out  
<sup>261</sup> that while the CPCP and integrated FAC have significant differences visual comparison  
<sup>262</sup> of the FAC and CPCP patterns show considerable agreement between the location of the  
<sup>263</sup> currents and the alignment of the convection pattern.

<sup>264</sup> After this short period of southward IMF, the IMF turns northward and the disparity  
<sup>265</sup> between the two simulations is reduced until the next interval of southward IMF arrives at  
<sup>266</sup> 07:40 UT. With short excursions northward this period of strong driving last until roughly

267 10:00 UT. During the majority of this interval the IMF is typically less than -12 nT. Figure  
268 3 shows the comparison between the baseline and ET runs at 09:00 UT which is in the  
269 middle of the interval of strong driving and corresponds to the largest difference between  
270 the CPCP seen in Figure 4. While there isn't much difference in the maximum in the  
271 Hall or Pedersen conductance at this time there is a clear and significant difference in the  
272 conductance patterns. The lack of difference between the maximum is due to the fact that  
273 the largest conductance in the baseline simulation is occurring in region just before dawn  
274 while the similar magnitude maximum is occurring throughout the dusk side in the ET  
275 results. The region of significant enhancement in conductance, roughly 3-4 [S] begins near  
276 12 MLT and extends to 19 MLT. The high conductivity occurs approximately 15 degrees  
277 colatitude and maps to the region between the R1 and R2 currents evident in the FAC  
278 patterns. This corresponds to regions of strong electric fields resulting from the current  
279 closure. This enhancement is evident in both the Pedersen and Hall conductance panels.  
280 A similar enhancement of of the conductance in pre-noon sector. It is occurring at lower  
281 latitudes, but still maps to area between the R1 and R2 currents in that sector. There  
282 is also an enhancement of the conductance across 00 MLT occurring at high latitudes.  
283 It's worth noting that the while the CPCP come into rough agreement during the short  
284 northward excursion of the IMF the integrated FAC are different through and largest at  
285 the end of the interval.

286 As the storm progress throughout the remainder of the day on March 17th there are  
287 intervals during the CPCP in the ET run is significantly less than in the baseline sim-  
288 ulation. Most notable of these are the periods 13:30-14:35 and 15:45-19:30 UT. Both  
289 intervals correspond to regions of southward IMF around -7 nT. In the first period the

<sup>290</sup> solar speed is near 700 km/s and in the second interval it declines from 625 to 600 km/s.  
<sup>291</sup> Examination of the scientific visualization during these intervals reveals structures similar  
<sup>292</sup> those shown in Figure 3, especially in the enhancements in on the dusk side and pre-noon  
<sup>293</sup> sector between the R1 and R2 currents. It is also instructive to examine the ionospheric  
<sup>294</sup> patterns at times when there is not a significant difference between the CPCP during the  
<sup>295</sup> decline phase of the geomagnetic storm. At 13:26 UT, the CPCP and integrated FAC are  
<sup>296</sup> nearly the same at 180 kV and 9 MA respectively. The conductance patterns are nearly  
<sup>297</sup> the same as well with a 1 [S] difference in the maximum values and enhancement in the  
<sup>298</sup> conductance in the pre- and post-noon sectors between the R1 and R2 currents.

<sup>299</sup> As a final comparison between the two simulation results we turn our attention the the  
<sup>300</sup>  $D_{ST}$  during the geomagnetic storm. Both simulations show and positive enhancement of  
<sup>301</sup>  $D_{ST}$  at the arrival of the shock. Between 06:20 and 08:30 UT the simulated  $D_{ST}$  indices  
<sup>302</sup> follow roughly the same path of decreasing value. Both simulations reach a minimum  
<sup>303</sup>  $D_{ST}$  value around 09 UT, but the ET value is 25 nT less than the value obtained by the  
<sup>304</sup> baseline run. Both simulations reach the minimum value about 90 minutes before the  
<sup>305</sup> observations. The 25 nT offset between the ET and baseline runs persists through the  
<sup>306</sup> remainder of the storm. In the later phases of the storm the observed values come closest  
<sup>307</sup> to the observations. While not shown here, it is worth pointing out as *Li et al.* [2016] did  
<sup>308</sup> that LFM-RCM simulations produce a significantly better agreement between  $D_{ST}$  than  
<sup>309</sup> stand-alone LFM simulations.

### 3.2. Comparison with DSMP

<sup>310</sup> So far the majority results shown have only contrasted the two simulation results. While  
<sup>311</sup> this is instructive and illustrates the impact the inclusion of the ET terms is having on

simulation results it does not provide any verification that new results are better than the previous simulation results. We begin that process by comparing the two simulation results with observations made by the DMSP spacecraft. Figure 5 shows the DMSP F17 and F18 trajectories during two intervals occurring in the main phase of the geomagnetic storm. The spacecraft were orbiting across the dusk-dawn meridian, measuring the horizontal component of ion drift velocity at altitude of approximately 830?km together with fluxes of magnetospheric particle precipitating. The first pass occurring between 09:45 and 10:45 UT corresponds to the results shown in Figure 3 and are at a time of significant difference between the two model results. During the second pass, 11:25 - 12:30 UT the difference between the simulation results is less.

The panels a and c of Figure 6 show comparisons on the cross-track ion drift velocity between the DMSP measurements and the simulations along two consecutive orbits of the F17 spacecraft over the northern hemisphere, orbiting from the duskside to dawnside across the polar region. The velocity shown in Figure 6 is perpendicular to the satellite trajectory, with positive values for anti-sunward convection and negative values for sunward convection. As indicated by the measured drift velocity in Figure 6, the DMSP F17 satellite passes through the regions of two-cell convection with sunward drift in the dusk sector, followed by anti-sunward drift over the polar cap and sunward drift in the dawn sector. The b and d of Figure 6 show the measured spectrum of electron and ion precipitation. The measured equatorward boundaries of the auroral oval are indicated using black dashed lines in each panel based on the sharp gradient in the observed electron spectrum. According to the DMSP drift velocity and particle measurements, the observed double-channel profiles of the westward drift velocity on the dusk side (near 9:59 and 11:41

335 UT) are separated by the auroral precipitation boundary in both cases, indicating that  
336 the lower latitude westward plasma flow is in the subauroral region, which is also known  
337 as sub-auroral polarization streams (SAPS). The comparisons on the cross-track plasma  
338 drift velocity suggest that the coupled LFM-RCM model is capable of reproducing the  
339 large-scale two-cell convection velocity profiles observed along the two consecutive DMSP  
340 F17 trajectories. As indicated by the boundaries of the simulated auroral energy flux the  
341 spatial extension of the simulated auroral oval resembles the observations during the two  
342 F17 passes. Combined with the simulated velocity profiles, the LFM-RCM model is also  
343 capable of reproducing the magnitude of the observed fast plasma flow in the subauroral  
344 region (during 09:54-10:00 and 11:34-11:40) with little particle precipitation fluxes.

345 A similar comparison between the LFM-RCM simulation and the measurements from  
346 two consecutive DMSP F18 passes during the main phase of the storm is shown in Figure  
347 7. The LFM-RCM model is capable of reproducing the double-channel convection pro-  
348 files during both F18 trajectories between 10:09-10-18 and 11:54-12:03 UT, respectively,  
349 although the simulated peak location of the subauroral flow channel is a couple of degrees  
350 MLAT poleward compared to the measured SAPS features especially during the second  
351 F18 pass. It is possible that the location discrepancies in the SAPS channel between the  
352 LFM-RCM simulation and DMSP observations are due to the fact that the auroral oval  
353 in the LFM-RCM simulation is several degrees of MLAT poleward compared to the mea-  
354 sured particle spectrum. The disagreement in the location of the auroral oval is likely a  
355 consequence of the fact that the distribution of upward Region 1 field-aligned currents in  
356 the global simulation is several degrees in MLAT poleward compared to observations (ref-  
357 erence Zhang et al., 2011, or comparison with Weimer in this paper?). Note that on the

358 downside, the LFM-RCM simulation misses the channels of anti-sunward flow observed  
359 by the two DMSP F18 passes near 10:27 and 12:12 UT, which is possibly due to the fact  
360 that the simulated high-latitude convection pattern in LFM-RCM is more contract than  
361 the measurements in the morning sector (reference to the statistical study?).

### 3.3. Comparison with AMPERE

362 Now we move onto a comparison of the simulation results with the observations of the  
363 FAC patterns obtained from the AMPERE mission. The second scientific visualization  
364 accompanying this paper makes this comparison by plotting the patterns of the northern  
365 hemisphere currents along with cuts along specific MLTs. Figure 8 is extracted from this  
366 visualization at 09:00 UT on March 17th. The top row in the visualization provides a  
367 comparison of the FAC patterns for the northern hemisphere from the simulation and  
368 the AMPERE reconstruction. A two minute cadence was adopted for this visualization  
369 to match the highest output frequency available for the AMPERE observations. It is  
370 important to note that the AMPERE observations are built up over a 10 minute averaging  
371 window and that average is being compared with an instantaneous value obtain from the  
372 MIX output. *Slava - Please confirm that my description of the AMPERE reconstruction*  
373 *method is correct.* In order to allow for a more quantitative comparison the bottom row of  
374 the visualization contains cuts from the current densities at several magnetic local times.  
375 Panels d and f provide cuts through the morning and afternoon sectors while panel e  
376 provides a cut from dusk to dawn.

377 As discussed in Section 3.1 prior to the arrival of the shock the solar wind driving of  
378 the magnetosphere is quite weak. At 03:00 UT the solar IMF is mainly northward and  
379 a careful examination of the FAC patterns at this time shows an NBZ current system

380 in both simulation results. The faint trace of an NBZ current system is apparent in  
381 the afternoon sector. These patterns can be hard to see in the visualization since the  
382 range of the color bar was selected to capture times when strong currents are flowing.  
383 Turning our attention to the MLT comparisons we see that for the 09 and 15 MLT cuts  
384 the two simulation results are virtually identical. Differences can be seen in the 18 MLT  
385 portion of the dawn-dusk cut, due the current in the ET version extending slightly more  
386 anti-sunward. The NBZ current systems do not appear in the AMPERE reconstruction,  
387 especially since a threshold value of  $0.15 \mu Am^{-2}$  is needed for the currents to above the  
388 noise threshold. The strong level agreement between the two simulations is not surprising  
389 since the ET effects are not likely to occur at this point in the simulation.

390 Next we focus our attention at 09:00 UT shown in Figure 8 that corresponds to time  
391 with the largest differences in CPCP seen between the two simulation results and is  
392 occurring at time of strong driving of the magnetosphere. While the difference between  
393 the CPCP is largest at this time there is a striking level of similarity in the FAC patterns  
394 for the two simulations. Across the entire days side the location, width, and strengths of  
395 the R1 and R2 currents are quite similar. There is a notable difference on the nightside  
396 with the baseline simulation have stronger FAC pairs in the midnight sector. Also the  
397 peaks in the R1 currents that occur below the 18-06 MLT line are stronger in the baseline  
398 simulation. The strength of the currents is stronger than those seen in the AMPERE  
399 results. The R1 and R2 currents also appear to be at higher latitudes than those seen in  
400 the AMPERE results. The weaker currents in the AMPERE results has been reported  
401 before by *Merkin et al. [2013]* and is result of the fitting process underestimating the true  
402 current strength. Looking at the 15 MLT comparison we see that the strength of currents

403 along this cut is the same in the baseline and ET simulations. The current peaks are  
404 higher and about a 1-2 degrees higher in latitude. There is also a high latitude feature in  
405 the AMPERE current observations that does not appear in either simulation result. In  
406 the 09 MLT there is a 1-2 degree difference in the location of the peak current between  
407 the two simulation results. The current peaks appear to bracket the observed current  
408 peak with the baseline simulation peak at above the AMPERE peak and the ET peak  
409 below it. The peak current here is about a factor of two larger than the AMPERE results  
410 and the currents are wider. The wider currents in the simulation results are also seen in  
411 the 18-06 MLT cut. This especially clear for the currents in the 18 MLT line. Unlike the  
412 other currents reported here the AMPERE currents are stronger in this region than what  
413 is reported by AMPERE. Along the 06 MLT cut the currents return to being about a  
414 factor of 2 larger in the R1 location. Even though is this the time with largest difference  
415 in CPCP the differences between the two simulations is relatively modest and agree quite  
416 well with the AMPERE observations.

417 As previously noted as the storm progress through the remainder of the day there are  
418 intervals with strong driving a differences between the CPCP between the two simulations.  
419 The 14:00 UT frame is typical of the conditions during the 13:30-14:35 interval of strong  
420 driving. The modest 1-2 degree separation between the current peaks noted in the 09  
421 MLT cut of the 09:00 UT is present in all of the cuts through the currents. In general, the  
422 baseline simulation peak appears to be closer to the peak in the AMPERE observations.  
423 This trend is also apparent in the 15:45-19:30 UT interval of strong driving with the 16:12  
424 frame providing a clear example. Also notable in this frame are the strong peaks in the R1  
425 currents below the 18-06 MLT line in the ET simulation results. It is worth pointing out

426 that at 13:26 UT time, previously identified as an instant with little differences between  
427 the CPCP and integrated FAC there are very small differences between the two simulation  
428 results.

### 3.4. Comparison with TS07-D

429 Initial drafting of this section has been assigned to Slava.

430 May include a comparison with pressures in the in the ring current depending on length  
431 and quality of comparison.

## 4. Summary and Future Directions

432 Mike will write this section once the paper is nearly finished.

433 Our SAPS are the best!

434 **Acknowledgments.** This material is based upon work supported by NASA grants  
435 XX, YY, and ZZ. The National Center for Atmospheric Research is sponsored by the  
436 National Science Foundation. All model output, simulation codes, and analysis routines  
437 are being preserved on the NCAR High Performance Storage System and will be made  
438 available upon written request to the lead author of this publication.

## References

- 439 De Zeeuw, D. L., S. Sazykin, R. A. Wolf, T. I. Gombosi, A. J. Ridley, and G. Tóth (2004),  
440 Coupling of a global MHD code and an inner magnetospheric model: Initial results, *J.*  
441 *Geophys. Res.*, 109(A), 12,219.  
442 Dimant, Y. S., and G. M. Milikh (2003), Model of anomalous electron heating in the E  
443 region: 1. Basic theory, *Journal of Geophysical Research*, 108(A), 1350.

- 444 Dimant, Y. S., and M. M. Oppenheim (2011), Magnetosphere-ionosphere coupling through  
445 E region turbulence: 2. Anomalous conductivities and frictional heating, *Journal of*  
446 *Geophysical Research*, 116(A), A09,304–n/a.
- 447 Gallagher, D. L., P. D. Craven, and R. H. Comfort (2000), Global core plasma model, *J.*  
448 *Geophys. Res.*, 105, 18,819.
- 449 Glocer, A., M. Fok, X. Meng, G. Tóth, N. Buzulukova, S. Chen, and K. Lin (2013),  
450 CRCM + BATS-R-US two-way coupling, *J. Geophys. Res.*, 118(4), 1635–1650.
- 451 Goodrich, C. C., A. L. Sussman, J. G. Lyon, M. A. Shay, and P. A. Cassak (2004), The  
452 CISM code coupling strategy, *J. Atmos. Solar Terr. Phys.*, 66(1), 1469–1479.
- 453 Gurevich, A. V. (1978), Nonlinear phenomena in the ionosphere, *New York*, 10.
- 454 Hapgood, M. A. (1992), Space physics coordinate transformations - A user guide, *Plane-*  
455 *tary and Space Science (ISSN 0032-0633)*, 40, 711–717.
- 456 Li, Z., M. Hudson, J. Paral, M. Wiltberger, and D. Turner (2016), Global ULF wave  
457 analysis of radial diffusion coefficients using a global MHD model for the 17 March 2015  
458 storm, *J. Geophys. Res.*
- 459 Merkin, V. G., G. Milikh, K. Papadopoulos, J. Lyon, Y. S. Dimant, A. S. Sharma,  
460 C. Goodrich, and M. Wiltberger (2005), Effect of anomalous electron heating on the  
461 transpolar potential in the LFM global MHD model, *Geophysical Research Letters*,  
462 32(2), 22,101.
- 463 Merkin, V. G., B. J. Anderson, J. G. Lyon, H. Korth, M. Wiltberger, and T. Motoba  
464 (2013), Global evolution of Birkeland currents on 10 min timescales: MHD simulations  
465 and observations, *J. Geophys. Res.*, 118(8), 4977–4997.

- 466 Milikh, G. M., L. Goncharenko, Y. S. Dimant, J. P. Thayer, and M. A. McCready (2006),  
467 Anomalous electron heating and its effect on the electron density in the auroral elec-  
468 trojet, *Geophysical Research Letters*, 33(1), L13,809.
- 469 Oppenheim, M. (1996), A wave-driven nonlinear current in the E-region ionosphere, *Geo-*  
470 *physical Research Letters*, 23(2), 3333–3336.
- 471 Oppenheim, M. (1997), Evidence and effects of a wave-driven nonlinear current in the  
472 equatorial electrojet, *Annales Geophysicae*, 15(7), 899–907.
- 473 Oppenheim, M. M., and Y. S. Dimant (2013), Kinetic simulations of 3-D Farley-Buneman  
474 turbulence and anomalous electron heating, *J. Geophys. Res.*, 118(3), 1306–1318.
- 475 Pembroke, A., F. Toffoletto, S. Sazykin, M. Wiltberger, J. Lyon, V. Merkin, and  
476 P. Schmitt (2012), Initial results from a dynamic coupled magnetosphere-ionosphere-  
477 ring current model, *J. Geophys. Res.*, 117(A2).
- 478 Richmond, A. D. (1992), Assimilative mapping of ionospheric electrodynamics, *Adv. Space*  
479 *Res.*, 12(6), 59–68.
- 480 St Maurice, J. P. (1990), Electron heating by plasma waves in the high latitude E-region  
481 and related effects - Theory, *COSPAR*, 10(6), 239–249.
- 482 Tóth, G., et al. (2005), Space Weather Modeling Framework: A new tool for the space  
483 science community, *J. Geophys. Res.*, 110(A), 12,226.
- 484 Welling, D. T., and A. J. Ridley (2010), Validation of SWMF magnetic field and plasma,  
485 *Space Weather*, 8(3), 03,002.
- 486 Wiltberger, M., R. S. Weigel, W. Lotko, and J. A. Fedder (2009), Modeling seasonal  
487 variations of auroral particle precipitation in a global-scale magnetosphere-ionosphere  
488 simulation, *J. Geophys. Res.*, 114(A), 01,204.

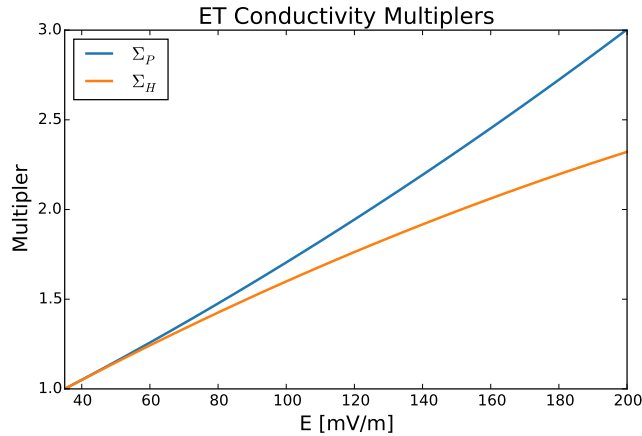


**Figure 1.** The conductivity multipliers for the Electrojet Turbulence effects. The blue curve is for the Pedersen conductance while the orange curve is for the Hall conductance. The effects occur for all values above 35 mV/m.

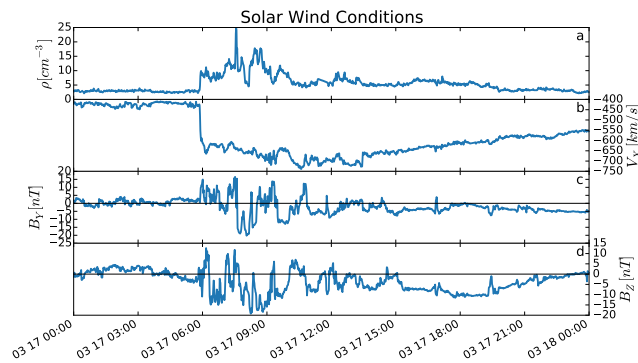


**Figure 2.** Solar wind and IMF conditions during the 17 March 2013 geomagnetic storm event. Panel a) shows the number density, b) the  $V_X$  in GSM coordinates. The IMF GSM Y and Z values are plotted in panels c) and d) respectively.

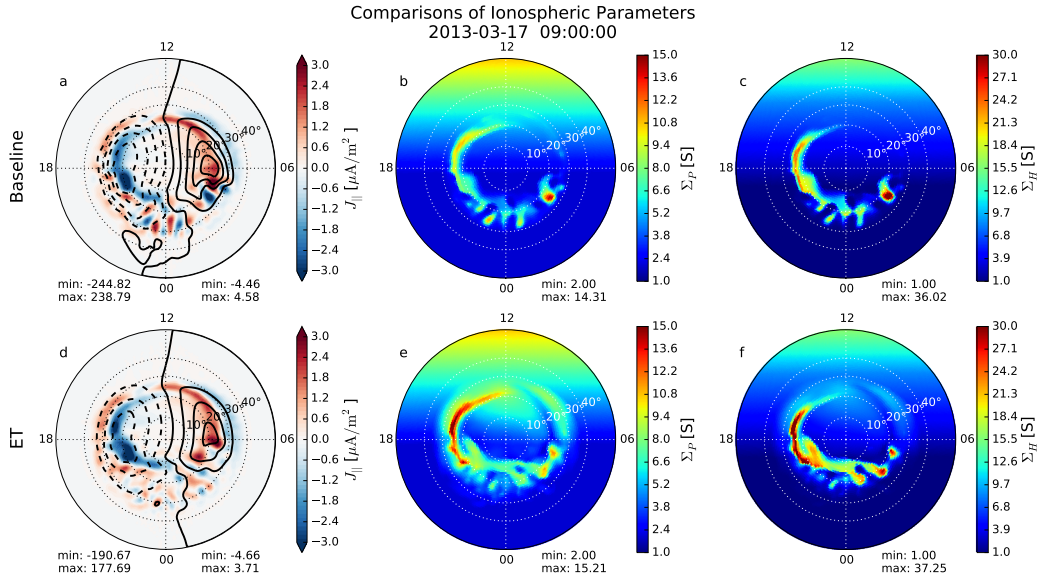


**Figure 3.** Frame from the scientific visualization showing of FAC and CPCP as well as Pedersen and Hall conductivities for the Baseline and ET simulations of the 17 March 2016 geomagnetic storm. The top row (panels a-c) contains the results from the baseline simulation while the bottom row (panels d-f) contains the results of the simulation with the ET enabled. The first column (panels a and d) has the FAC in color with blue being upward and red being downward as well as the CPCP pattern with 20 kV contours. The middle column (panels b and e) contains the Pedersen conductivity. The last column (panels c and f) contains the Hall conductivity. The color bar for the Pedersen conductance ranges from 1 to 15 [S] while the upper limit for the Hall conductance is 30 [S]

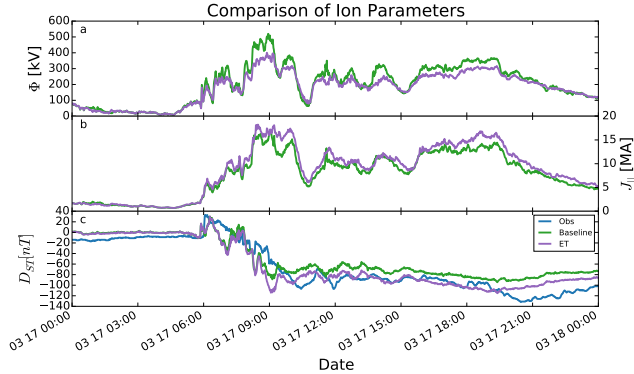


**Figure 4.** Comparison of the CPCP, FAC, and  $D_{ST}$  time series for the storm event for the Northern hemisphere. Panel a at the top shows the CPCP in kV. The middle panel (b) has the integrated FAC. Panel c at the bottom has the  $D_{ST}$  index. In each panel the LFM-RCM results are shown with the green line, the ET results with the purple line. In the bottom panel the  $D_{ST}$  obtained from CDAWeb is plotted in blue

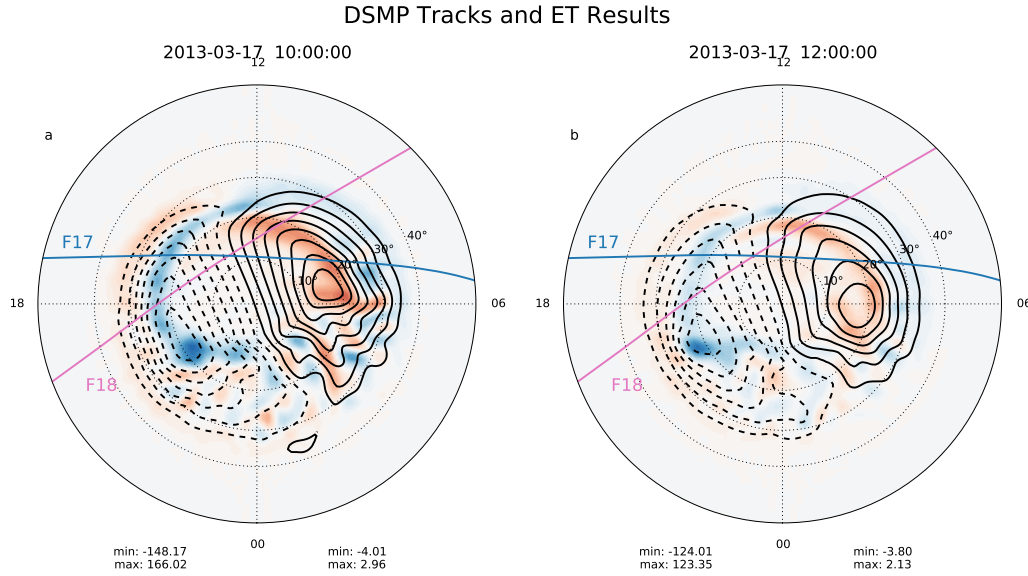


**Figure 5.** DSMP F17 and F18 trajectories overlaid on top of ET FAC and CPCP patterns. Panel a shows the F17 trajectory between 0945 and 1030 UT and the F18 trajectory between 1000 and 1045 UT overlaid on top of the ET simulation results for 10:00UT. Panel b shows the F17 trajectory between 1125 and 1210 UT and the F18 trajectory between 1145 and 1230 UT overlaid on top of the ET simulation results for 12:00UT. In each panel the F17 trajectory is blue and the F18 trajectory is pink.

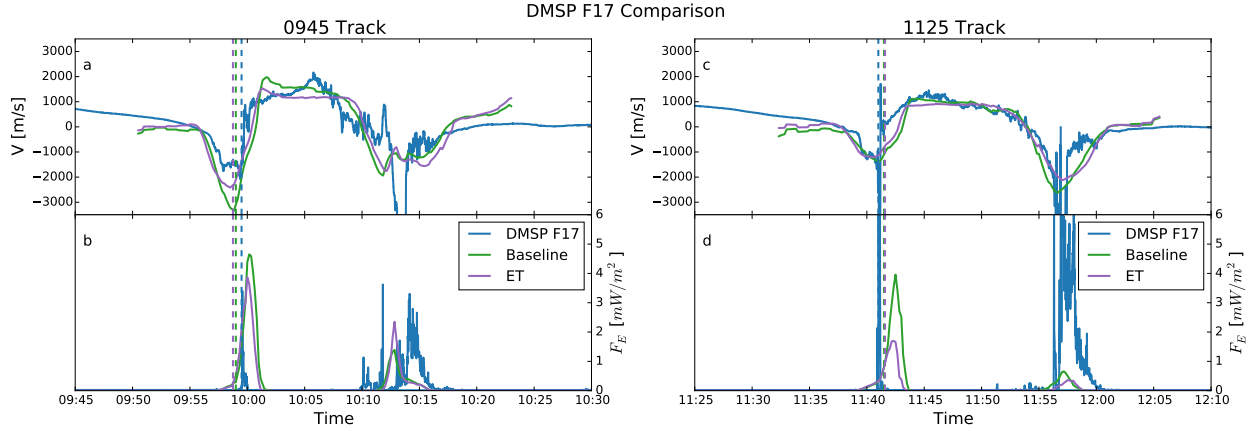


**Figure 6.** Comparison of DMSP F17 observations and simulation results. The first column, panels a and b, show the comparison for the 0945 pass. The second column, panels c and d, have the comparison for the 1125 pass. The first row, panels a and c, compare the cross track ion velocity from DMSP with the velocities obtained from the Baseline and ET simulations. The second row, panels b and d, compares the electron energy fluxes. In each panel the observations are shown in blue, the baseline results in green and ET results in purple.

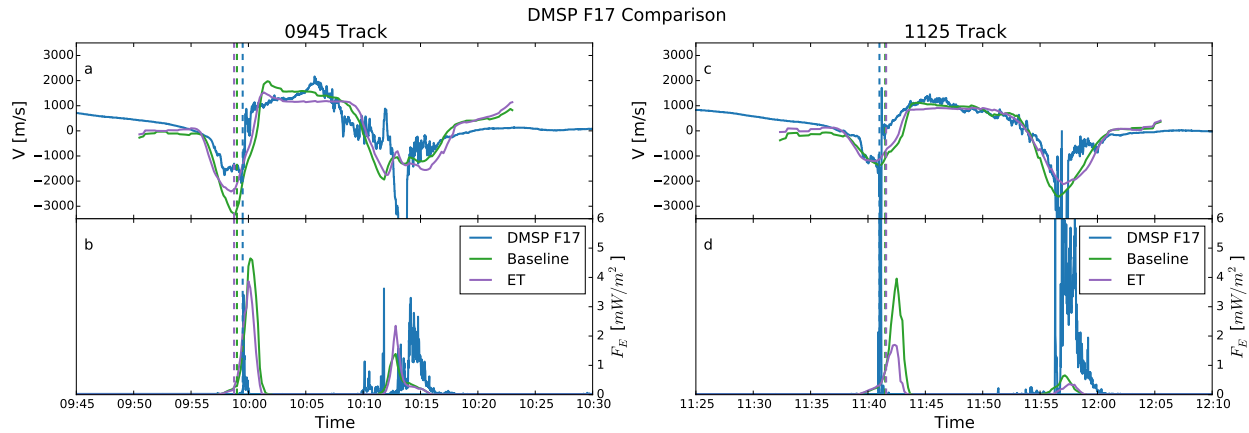


**Figure 7.** Comparison for DSMP F18 observations in the same format as Figure 6.

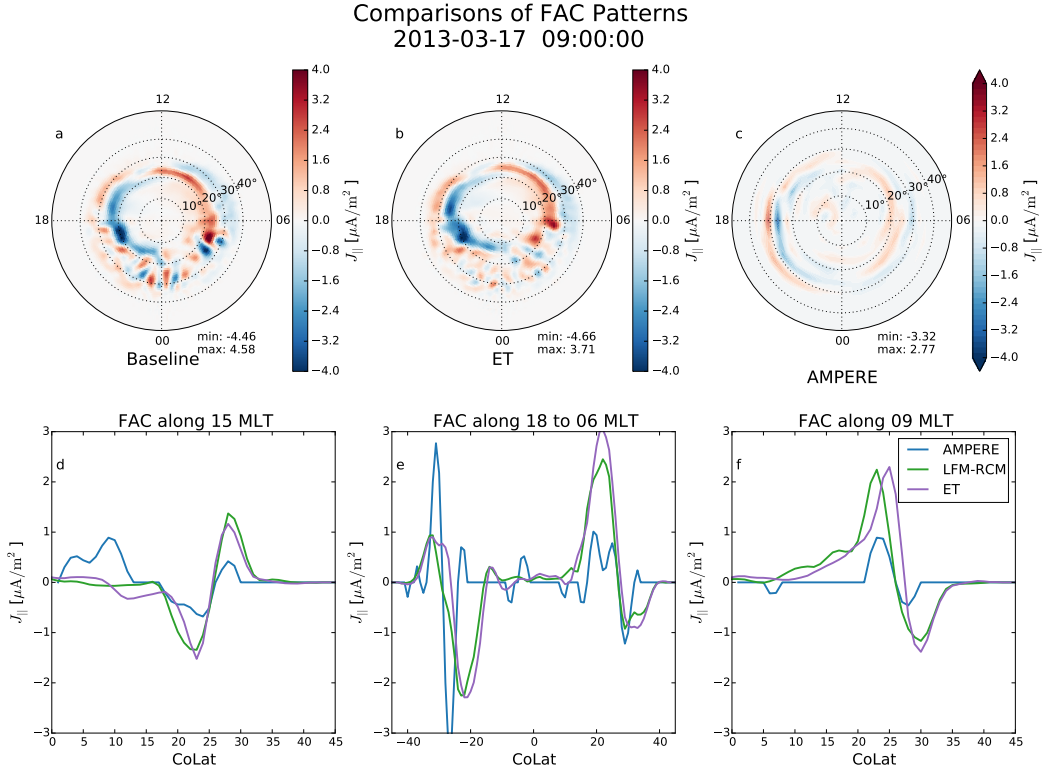


**Figure 8.** Frame extracted from the scientific visualization comparing the FAC from the simulations with the patterns derived from AMPERE magnetometer observations. The top row, panels a-c, shows the FAC patterns for the northern hemisphere using the same color bar. Panel a is the baseline simulation, panel b is the from the Electrojet Turbulence simulation and panel c is from the AMPERE observations. The bottom row makes comparisons of current strengths along cuts in MLT. Panel d is a cut along 15 MLT and extends from 0-45 degrees colatitude. Panel f is cut along 09 MLT and has the same range as panel a. Panel e is a cut along the 18 and 06 MLT line. In this plot the negative colatitude values correspond to locations along the 18 MLT line, while the positive values are along the 06 MLT line. This plot gives a cut from dusk to dawn in a single panel. In all the comparison plots the AMPERE observations are shown in blue, the baseline simulation in green and the ET simulation in purple.

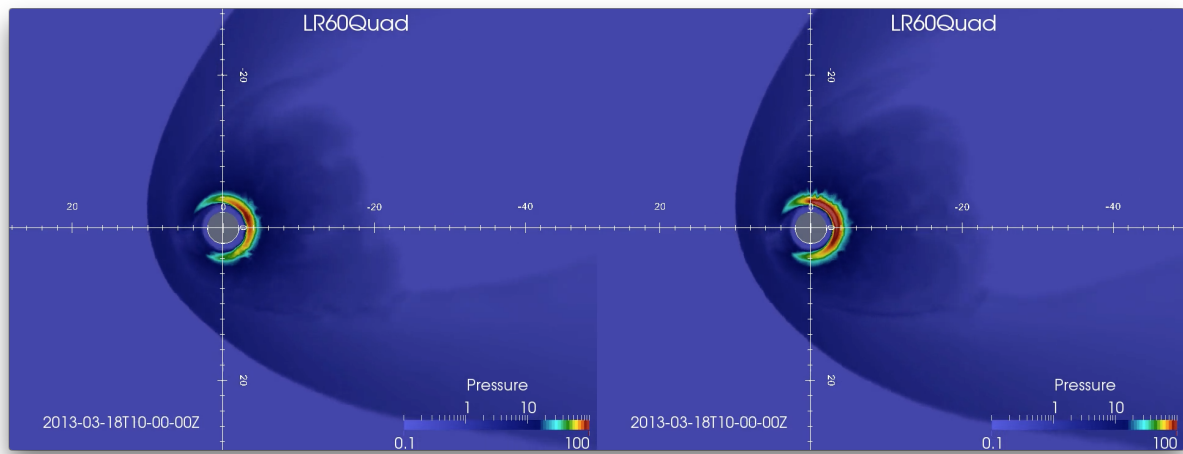


**Figure 9.** Temporary Figure comparing Baseline and ET pressures